Catalysis Today xxx (xxxx) xxx–xxx

Contents lists available at ScienceDirect

Catalysis Today

journal homepage: www.elsevier.com/locate/cattod

Highly active oxygen evolution reaction model electrode based on supported gas-phase NiFe clusters

Lisa Geerts[a], Salvatore Cosentino[b], Ting-Wei Liao[b], Anupam Yadav[b], Pin-Cheng Lin[c], Vyacheslav S. Zharinov[b], Kuo-Juei Hu[b], Alessandro Longo[d,e], Lino M.C. Pereira[c], Didier Grandjean[b], Jan Rongé[a], Peter Lievens[b], Johan A. Martens[a,*]

[a] KU Leuven, Center for Surface Chemistry and Catalysis, Celestijnenlaan 200F, 3001 Leuven, Belgium
[b] KU Leuven, Laboratory of Solid-State Physics and Magnetism, Celestijnenlaan 200D, 3001 Leuven, Belgium
[c] KU Leuven, Institute for Nuclear and Radiation Physics, Celestijnenlaan 200D, 3001 Leuven, Belgium
[d] Netherlands Organization for Scientific Research (NWO), Dutch-Belgian Beamline, ESRF - The European Synchrotron, CS40220, 38043, 71 Avenue des Martyrs, 38000 Grenoble, France
[e] Institute of Nanostructured Materials (ISMN)-CNR, UOS Palermo, Via Ugo La Malfa, 153, 90146 Palermo, Italy

ARTICLE INFO

Keywords:
Gas-phase cluster
Cluster beam deposition
Oxygen evolution reaction
Nickel-iron

ABSTRACT

Under alkaline conditions mixed NiFe oxides/oxyhydroxides are among the most active catalysts for the oxygen evolution reaction (OER). Here we investigate $Ni_{0.5}Fe_{0.5}$ clusters as a well-defined model highly active electrocatalyst system for the OER. The electrodes were prepared using gas-phase deposition of mixed $Ni_{0.5}Fe_{0.5}$ metallic clusters produced by cluster beam deposition (CBD), a technique offering precise control of composition and loading. Highly dispersed $Ni_{0.5}Fe_{0.5}$ clusters were deposited at 1 equivalent monolayer and used as OER catalyst in 1 M KOH. The low loading allows assessment of the intrinsic catalytic activity and their extensive structural characterization by XAFS and XPS spectroscopies. $Ni_{0.5}Fe_{0.5}$ clusters demonstrate high stability as there is no apparent potential increase after a 12 h constant current density anodization test. After electrochemical aging, the lowest overpotential was achieved and amounts to 372 mV at 10 mA cm^{-2}. The Tafel slope reaches 37 mV dec^{-1}. The measured electrochemical activity is also compared with other systems. After OER reaction in KOH the cluster surface is enriched in NiOOH, while concomitant Fe depletion from the catalyst surface is observed. These findings help to shed light on the formed active phase at the nanoscale.

1. Introduction

A transition to a sustainable and environmentally friendly energy economy is the need of the hour as the problems we face today, air pollution and climate change, are associated with the combustion of fossil fuels. In this regard, there is growing interest in hydrogen production by water electrolysis for storing solar and wind energy in a chemical form [1–4]. The efficiency of hydrogen production is limited in large part by the slow kinetics of the oxygen evolution reaction (OER) at the anode. The most promising OER catalysts based on earth-abundant elements are oxides/hydroxides containing both Ni and Fe [1,5–11]. They are operated in alkaline electrolytes in order to avoid corrosion. Mixed NiFe (oxy)hydroxides with Ni in majority and containing 10 − 50% Fe have been reported to have the highest OER activities [6,10,12,13]. These high activities have been reproduced, but the material itself remains poorly defined and its redox behavior and optimal structure and composition are not well understood [14,15]. Other first-row transition metal oxides that are promising due to its high OER activity are cobalt-based electrocatalysts [9,16–18]. Also ternary combinations with a metal such as Cr have been shown to increase the activity of NiFe oxides/oxyhydroxides [19,20].

Mixed metals, oxides and (oxy)hydroxides containing Ni and Fe have been synthesized via a variety of chemical and physical routes. A widely employed method is electrodeposition, predominantly producing amorphous or poorly crystallized (oxy)hydroxide films [14,17]. Co-precipitation and solvo- and hydrothermal methods are common methods to obtain NiFe layered double hydroxide (LDH) powders [1,11]. Also oxide powders have been reported with the hydrothermal method [21]. Solution casting generates uniform oxide films, while reactive sputter deposition and thermal evaporation result in metallic films that are subsequently oxidized [2,6,22,23]. Mixed NiFe catalyst powders have also been produced by mechanical alloying, consisting in

* Corresponding author.
E-mail address: johan.martens@kuleuven.be (J.A. Martens).

https://doi.org/10.1016/j.cattod.2019.01.062
Received 1 July 2018; Received in revised form 17 January 2019; Accepted 25 January 2019
0920-5861/

mixing of elemental powders [24]. Solid-state reactions produce oxide nanoparticles [1,14,25,26]. Mixed metal hydroxide catalysts for OER have been obtained by pulsed-laser ablation in liquid, which generally results in crystalline nanomaterials [27]. Furthermore, exfoliation of layered metal hydroxides leads to single-layer nanosheets with enhanced OER activity [3]. Other alternative methods including an aerosol-spray-assisted approach and photochemical metal-organic deposition produce amorphous metal oxide materials [28,29]. These methods produce catalysts that differ in crystal size, phase, crystallinity, morphology,… all of which are parameters affecting the electrocatalytic activity.

Moreover, OER catalysts are dynamic under operating conditions. Fe incorporation due to impurities in the electrolyte and changing phases under operating potentials make it difficult to relate the structural and compositional features to its activity trends [10,11,30,31]. Under OER conditions in alkaline environment, the active phase that usually forms is the oxyhydroxide phase, which has been reported previously and is consistent with the Pourbaix diagram [2,7,14,30,32]. Therefore some authors refer to these materials as (oxy)hydroxides, denoted by $NiFeO_xH_y$ as general formula without explicit description of the oxidation or protonation state that changes with both pH and potential [7,30,33].

The measured activity is however also highly dependent on a number of other factors such as the chemical composition, metal loading and electrochemically active surface area [1,2,7,14]. Only recently, the influence of the electron conductivity and mass transport limitations on the activity were addressed. In some cases, the substrate has been reported to have a positive effect on the activity, however the degree of enhancement is poorly understood [1,5,14,34]. These factors complicate identification of optimal structural and compositional characteristics needed for high activity.

To improve the understanding of the influence of the structural and compositional properties on the activity, we here study the intrinsic activity of well-defined catalytic nanoparticles deposited on a flat conductive support. Nanoparticles are attractive model systems for studying catalytic processes, because ohmic resistances, which are difficult to correct for, are minimized. Electrons only need to move short distances to reach the underlying electrode, which means that limited electric conductivity of the nanoparticles will not have major influences on the activity. In addition, mass transport of gases and ions will not significantly affect the activity as no porous structure is involved and the material loading is low [14,35]. For practical water splitting devices however, where higher loadings are desired, it is beneficial to deposit the catalyst on a conductive 3D high-surface area support. A 3D support maximizes the exposed active sites and facilitates mass and bubble transport [35,36]. For example, carbon cloth is a cheap 3D support with high conductivity and excellent flexibility [37,38].

Here we report a new way of preparing mixed bimetallic Ni_xFe_{1-x} OER electrocatalyst layers composed of individual nanoclusters, produced in gas-phase via laser ablation in a cluster beam deposition (CBD) setup [39,40]. A laser was used to ablate a mixed bulk NiFe target with 1:1 ratio to generate atom vaporization and to form $Ni_{0.5}Fe_{0.5}$ clusters. Two laser beams can also be used to ablate two bulk targets of Ni and Fe and in this way different compositions can be achieved by tuning the power of the lasers [41]. This technique results in a high uniformity and superior control over composition and loading of the electrocatalyst, which makes it convenient for preparing model catalysts for investigating OER activity. In comparison with clusters deposited from chemical precursors in solution; particle size, coverage and composition can be more precisely controlled in a very flexible way [42,43]. All samples were deposited at 1 equivalent atomic monolayer (ML) of NiFe clusters, corresponding to around 1.98×10^{15} atoms cm^{-2}. Thereafter the OER catalytic activity in 1 M KOH was investigated. Steady state measurements and electrochemical impedance spectroscopy (EIS) were used to measure kinetically significant parameters such as the Tafel slope. The ultra-low loading allows calculation of intrinsic catalytic activity parameters. Extensive characterization of the structural and electronic properties of the deposited clusters before and after the catalytic reaction was conducted using microscopic and x-ray spectroscopic techniques.

2. Material and methods

2.1. Substrates

$Ni_{0.5}Fe_{0.5}$ cluster electrodes were fabricated on flat substrates: SiO_2/Si, Au/C TEM grid, Au/Si and fluorine-doped tin oxide (FTO) coated glass slides (Aldrich) with 10 Ω/sq surface resistivity. The Au/Si substrate was obtained via sputtering on a wafer. n-type silicon wafers (Cemat Silicon, 4″ unpolished, $3 - 10\,\Omega\,cm$) with a thickness of $525 - 575\,\mu m$ were used. RCA cleaning was followed by wet oxidation at 1100 °C for 2 h to obtain an insulating layer of SiO_2 on both sides of the wafer. Thin films were sputtered using Balzers BAE 370 sputtering tool. First, a Ti/W($Ti_{0.1}W_{0.9}$ target, 99.95%) adhesion layer was sputtered at 2×10^{-3} mbar Ar and 150 W for 1 min. Then Au (Au target, 99.99%) was sputtered at 50 W for 5 min, other parameters unchanged. The FTO samples were cut in pieces of 2.5 by 1.5 cm.

2.2. Cluster deposition

Prior to cluster deposition, the surfaces were cleaned with acetone, isopropyl alcohol and deionized water, sequentially. A series of monodispersed NiFe clusters were produced under UHV conditions (base pressure as low as 1×10^{-9} mbar) through a laser ablation cluster beam deposition (CBD) setup [39,40]. A Nd:YAG-laser beam (wavelength 532 nm, power 200–300 mW) was used to ablate a mixed target of Ni and Fe (1:1 ratio, 99.95% pure, ACI alloy) and to create atom vaporization. Simultaneous with the ablation laser pulses, a high pressure pulsed beam of He cooled with liquid N_2 was introduced in the source. This increase in partial pressure triggers cluster formation. Different compositions can be achieved by using two lasers and two separate pure targets. By tuning the power of the lasers ablating Ni and Fe targets, the composition can be varied [41]. The beam of clusters was then guided via an extraction chamber to the deposition stage in soft-landing conditions with low kinetic energy (˜0.5 eV/atom) on the substrates. Clusters extracted without any mass selection result in a homogeneous circular beam of clusters (˜90% being neutral, ˜5% positively charged, ˜5% negatively charged) with a diameter of 1 cm.

2.3. Cluster characterization

The size distribution of clusters was evaluated by in-situ Reflectron Time-of-Flight mass spectrometry, by considering mass distribution (m/z) signal of cationic (single positive charged) clusters. Conversion of the spectra from m/z distribution to cluster size distribution is based on the assumption of a spherical shape for the clusters with size:

$$d_{cluster} = 2\left(\frac{m/z}{m_{at}}\right)^{\frac{1}{3}} r_{at}$$

where m_{at} is the atomic mass in u and r_{at} is the atomic Wigneir-Seitz radius of the element (0.138 nm for Ni and 0.141 nm for Fe atom).

The amount of deposited clusters was measured during deposition through a calibrated quartz crystal microbalance (QCM). All samples were deposited with 1 equivalent atomic monolayer (ML) of NiFe clusters, corresponding to around 1.98×10^{15} atoms/cm^2. The atomic ratio of NiFe alloy was determined by Rutherford backscattering spectrometry (RBS, 2.0 MeV He^+ beam, 166° backscattering angle) on samples deposited on SiO_2/Si substrate. Moreover, ex-situ scanning transmission electron microscopy (STEM) analysis in high angle annular dark field (HAADF) was performed on $Ni_{0.5}Fe_{0.5}$ clusters deposited on Au/C TEM grid. STEM analysis was performed with a probe-

corrected JEOL JEM ARM-200F microscope operating at 200 kV. Scanning electron microscopy (SEM) was performed with Raith GmbH EBL system with Zeiss GEMINI optical column on samples deposited on FTO substrates.

X-ray absorption fine structure (XAFS) data of clusters deposited on SiO_2/Si were collected at the Dutch-Belgian Beamline DUBBLE (BM26 A) of The European Synchrotron, operating in 7/8 + 1 mode, with a current of 160–200 mA [44]. Data were collected up to $k = 10.5\ Å^{-1}$ wave number with typical acquisition times of 25 min (i.e. 1–6 s per data point). Three spectra were averaged to improve the signal to noise ratio for the samples collected in fluorescence mode using a 9-channel Ge detector. Data reduction of the experimental X-ray absorption spectra was performed with the program EXBROOK [45]. Background subtraction and normalization was carried out by fitting (i) a linear polynomial to the pre-edge region in order to remove any instrumental background and (ii) cubic splines simulating the absorption coefficient from an isolated atom to the post-edge region. EXAFS refinements were performed with the EXCURVE package. Phase shifts and backscattering factors were calculated ab initio using Hedin-Lundqvist potentials.

Clusters deposited on Au thin film substrates (Au/Si) were characterized by XPS before and after the OER reaction to reveal and follow the oxidation state evolution and the atomic rearrangement of Ni and Fe in the $Ni_{0.5}Fe_{0.5}$ bimetallic clusters. After cluster deposition, the samples were directly transferred to the XPS setup with base pressure 2×10^{-9} mbar, and the binding energy of Ni 2p, Fe 2p, O 1 s and Au 4f was studied with a Mg Kα X-ray source (1253.6 eV with linewidth 680 meV). The kinetic energy of the photoelectrons emitted from the sample surface were collected with 25 eV pass energy by an electron energy analyzer in CAE mode. The Au $4f_{7/2}$ was selected as calibration peak and aligned to 84.0 eV. The deconvolution and fitting of the peaks were carried out with Unifit software.

2.4. Electrochemical methods

After cluster deposition, a conducting Cu wire (Conrad, 0.14 mm^2) was glued on the surface of the substrate with silver paint (RS Components) and the contact was entirely covered with epoxy resin (Loctite M-121MP Hysol, Henkel). Current-voltage curves were recorded at ambient temperature using a VersaSTAT 4 potentiostat (Princeton Applied Research) in a one-compartment electrochemical cell with electrolyte content of approximately 600 ml. A platinum coil (Bio-Logic) and an Ag/AgCl (3 M KCl saturated with AgCl, Radiometer Analytical) served as counter and reference electrode, respectively. 1 M KOH electrolyte was prepared using Milli-Q water (18 MΩ cm). O_2 was purged through the solution during the electrochemical measurements and the solution was stirred. The catalyst was electrochemically characterized using the following sequence of experiments: 1) Electrochemical Impedance Spectroscopy (EIS), 2) cyclic voltammetry (CV), 3) EIS, 4) Tafel analysis (chronopotentiometry), 4) EIS, 5) chronoamperometry (10 min) 5) CV and (6) chronopotentiometry (12 h). For each CV experiment, the scan rate was set at 10 mV/s. The Tafel analysis consisted of chronopotentiometry steps from 0.01 mA cm^{-2} to 10 mA cm^{-2}, each held for 3 min. The first two steps were held for 10 min. The measured potentials during the last minute of each Tafel step were averaged for plotting of the Tafel data. The impedance measurements were made at 0.85 V vs Ag/AgCl. Reported data were corrected for the uncompensated resistance (R_u) and current densities were normalized to the cluster-covered area. R_u was determined by performing potentiostatic EIS in a frequency region between 1 Hz and 1 MHz. R_u was extracted from the data in the high frequency region by determining the real part of the impedance where the phase angle was zero. R_u varied between 5.5 and 5.9 Ω. Geometric areas correspond to the spot size of the beam with a diameter of 1 cm. The measured potentials were converted to the potentials against the reversible hydrogen electrode (RHE) according to:

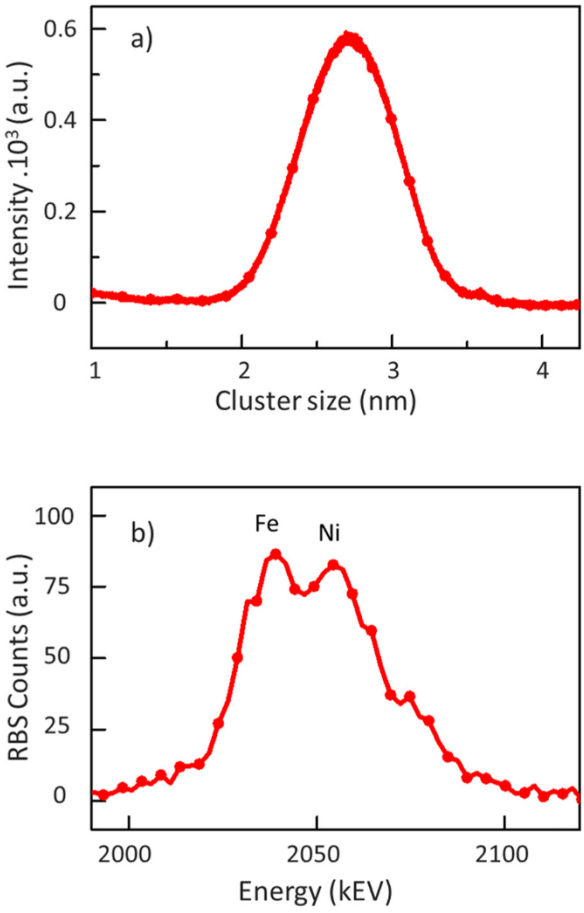

Fig. 1. a) Size distribution spectra of $Ni_{0.5}Fe_{0.5}$ clusters produced by the laser ablation cluster beam deposition setup. Conversion from Reflectron Time-of-Flight mass spectra to cluster size distribution is based on the assumption of a spherical shape of the clusters. The clusters have a diameter of 2.7 ± 0.7 nm. b) Rutherford Backscattering Spectroscopy spectrum of 1 ML $Ni_{0.5}Fe_{0.5}$ clusters on SiO_2/Si substrate. The area of the peak is proportional to the concentration of Ni and Fe atoms.

$$E_{RHE} = E_{Ag/AgCl} + E^0_{Ag/AgCl} + \ln 10 \frac{RT}{F} pH$$

where E_{RHE} and $E_{Ag/AgCl}$ are the potential of the working electrode with respect to the RHE and the reference electrode, respectively. $E^0_{Ag/AgCl}$ is the standard reduction potential of the reference electrode with respect to the standard hydrogen electrode. R, T, and F stand for the gas constant, temperature, and Faraday constant.

3. Results and discussion

3.1. Cluster deposition

In the CBD technique charged clusters produced in the source, together with post-ionized neutral clusters, are accelerated electrostatically and mass analyzed before their subsequent deposition on different supports [40]. Their size distribution was probed in situ during deposition with Reflectron Time-of-Flight mass spectrometry (RToF-MS). Fig. 1a shows the size distribution of the clusters. The abundance maximum corresponds to clusters with a diameter of 2.7 nm. Rutherford Backscattering Spectrometry (RBS) was used for compositional analysis of the clusters deposited on SiO_2/Si. The profile is given in Fig. 1b. The integrated area under the peak(s) determined using SIMNRA software shows that Fe and Ni RBS peaks have the same intensity [46]. As RBS intensity is proportional to the number of atoms and the atomic number square (NZ^2) and both elements have similar

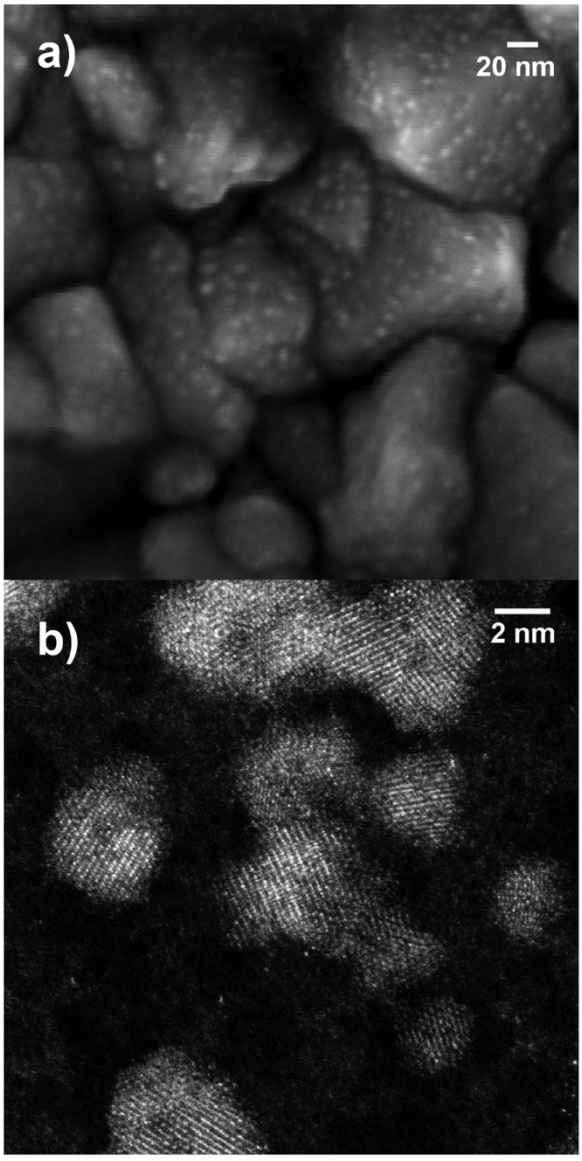

Fig. 2. SEM and HAADF-STEM images of the as-deposited $Ni_{0.5}Fe_{0.5}$ clusters: a) SEM image on FTO and b) HAADF-STEM image on Au/C TEM grid.

atomic numbers (Fe (26) and Ni (28)), this indicates that the Ni:Fe atomic ratio was 1:1.

Fig. 2a and b respectively are a scanning electron microscopy (SEM) image, using an in-lens detector, of the $Ni_{0.5}Fe_{0.5}$ clusters on the FTO substrate and a High-angle annular dark field scanning transmission electron microscopy (HAADF-STEM) image of the clusters on the Au/C TEM grid. As shown in Fig. 2a, the clusters cover uniformly the nano-textured surface of the FTO support, but are still spatially isolated from each other. Fig. 2b provides evidence that small isolated clusters with a size in the range of 2–3 nm were produced, because single clusters can be identified. Some clusters assemble to form larger agglomerates with a remarkable ring shape. Also, the clusters show some level of crystallinity.

Given the mean size of the clusters evaluated by reflectron time-of-flight mass spectrometry and STEM and the atomic amount measured by QCM and RBS, we estimate that the average density of clusters deposited on FTO is around 3×10^{12} clusters/cm^2 for all the investigated samples, corresponding to an overall mass of $Ni_{0.5}Fe_{0.5}$ clusters of around 0.17 μg/cm^2.

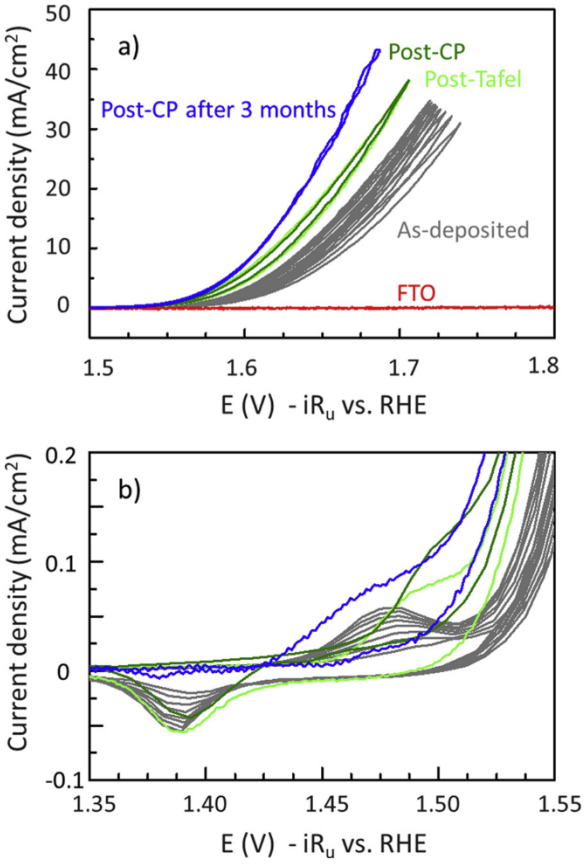

Fig. 3. a) Cyclic voltammograms of $Ni_{0.5}Fe_{0.5}$ clusters on FTO support, taken in 1 M KOH showing aging effects. Scan rate was set at 10 mV/s and the curves are corrected for the uncompensated resistance. The grey curves show the activity of the initial as-deposited clusters and the green scans are taken after steady-state Tafel analysis and after the chronopotentiometry experiment of 12 h aging at 10 mA/cm^2. The sequence of experiments was repeated with the same sample after 3 months. The blue curve shows the CV after the 12 h chronopotentiometry experiment. b) Zoomed-in region around the onset potential show the Ni^{2+}/Ni^{3+} redox peaks. The aged Ni films have a higher redox potential for the $Ni(OH)_2$/NiOOH transformation and a higher OER activity. (For interpretation of the references to colour in this figure legend, the reader is referred to the web version of this article).

3.2. OER activity and electrochemical aging

The OER electrocatalytic performance of the $Ni_{0.5}Fe_{0.5}$ cluster electrode in alkaline media is studied by cyclic voltammetry as shown in Fig. 3. Obtained potentials were converted to the reversible hydrogen electrode (RHE) reference. The results show clearly the OER activity of the $Ni_{0.5}Fe_{0.5}$ clusters as OER catalyst, as the FTO substrate is not active in the scanned potential region. In the first scan the catalyst reached a current density of 10 mA/cm^2 at 1.66 V *vs* RHE. In the high potential region, the OER activity increased with every subsequent cycle during initial cyclic voltammetry measurements. This has been previously attributed to two effects: 1) addition of Fe impurities from the electrolyte into NiOOH and 2) transformation of α-$Ni(OH)_2$/γ-NiOOH to β-$Ni(OH)_2$/β-NiOOH via aging [10,34]. Trotochaud et al. disputed the latter and stated that increase in OER activity can only be attributed to incorporation of Fe impurities from the electrolyte [5]. In this work, deposited metallic $Ni_{0.5}Fe_{0.5}$ clusters are used and show an aging transformation. We expect the metallic clusters to convert to the oxyhydroxide phase, consistent with the transformation reported in literature and Pourbaix diagrams [2,5,7]. This can also be appreciated by the redox peaks in the lower potential region, which have been previously attributed to the in situ transformation from $Ni(OH)_2$ to NiOOH

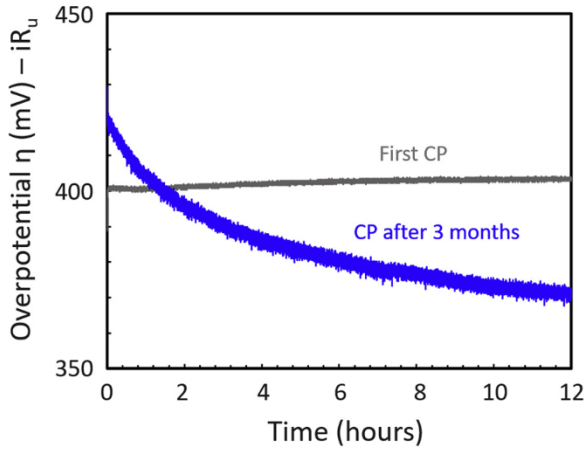

Fig. 4. Chronopotentiometry (CP) at a current density of 10 mA cm^{-2} of $Ni_{0.5}Fe_{0.5}$ on FTO. The blue curve shows the overpotential of the same sample after 3 months of storage (For interpretation of the references to colour in this figure legend, the reader is referred to the web version of this article).

phase [2,9,10,23,34]. Fig. 3b shows the redox peaks in more detail. The peak area was not constant and increased every cycle, which can be related to the increase in the amount of hydroxide phase, with respect to the initial metallic phase in the as-deposited clusters [23]. Also, the aged sample shows an anodic shift in the positions of the redox waves, a phenomenon previously observed for aged Ni and mixed NiFe catalysts [10,47–50]. After 3 months of dry storage, the same sequence of electrochemical tests was repeated on the same sample (Fig. S1 in supplementary). After 3 months, the same aging behavior was observed.

The long term stability of a catalyst is one of the most important requirements for a practical water splitting devices. A useful screening procedure for stability consists in running the electrodes at a current density of 10 mA cm^{-2} for several hours while potential changes are monitored [1,51]. Fig. 4 shows such a chronopotentiometry experiment. Because the overpotential after 12 h was only 3 mV larger than the initial value, the catalyst is considered stable during this period. The samples could also be stored for long time periods. After 3 months of dry storage the initial overpotential slightly increased by 30 mV. However, during the experiment the overpotential steadily decreased and reached 372 mV after 12 h, an improvement over the freshly prepared sample.

3.3. Intrinsic activity

The overpotential at the current density of 10 mA cm^{-2} is often used to compare various catalysts, corresponding to a solar-to-hydrogen conversion efficiency (STH) above 10% under 1 sun illumination [9,23,51]. However, as it is not normalized by the amount of material, it is difficult to compare the intrinsic activity of an active site. To address this important question, the turnover frequency (TOF) is often used [1]. The TOF is defined as the number of oxygen molecules produced per second and per active site:

$$TOF = \frac{I}{4\,F\,n}$$

where I is the measured current at a certain overpotential (A), F is the Faraday constant with a value of 96,485 C mol^{-1}, and n is the number of moles of active sites. We use the total metal mass and composition calculated from QCM and RBS for calculation of TOF and mass activity (A/g). The TOF is calculated assuming that all metal atoms in the clusters are active. To calculate the number of active sites, the conversion of cluster loading to the number of active sites n is done by using the molecular weight of Ni and Fe with the 50% Ni and 50% Fe ratio. The current at 300 mV overpotential (corrected for uncompensated resistance) is calculated by using steady-state Tafel plots and by averaging the forward and reverse of (20 moving-point averaged) CV scans taken at 10 mV/s. At very low mass loadings, high TOF values can be achieved close or equal to the material's intrinsic activity. When comparing TOF values to other catalysts reported in literature, care should be used because a variation in a number of parameters such as catalyst loading, electrochemical conditions and the definition of active site, can have a large effect on the overall activity [50]. Table 1 gives an overview of other low-loading electrodes measured in 1 M KOH. The TOF values in the table are based on the same assumption that all metal atoms in the catalyst are active. The number of moles of metal are calculated from QCM mass [2,14] and inductively coupled plasma optical emission spectroscopy (ICP-OES) [9].

The steady-state Tafel equation and CV experiment after 12 h of chronopotentiometry measurement were used to calculate the activity metrics. The Tafel slope deducted from the fit of the linear region of the data below 1 mA cm^{-2}, amounts to 37 mV dec^{-1} (Fig. S2 in SI), which is low taking into account the reported ranges between 25 and 70 mV dec^{-1} for NiFe-based catalysts [1,2,14,23,30,33,34]. The lowest overpotential of 372 mV was achieved after 12 h at 10 mA/cm^2. Lower values for overpotential have been reported for electrodes with higher metal loadings. In comparison to other physical deposition methods as in the work of Bisot-Peiro et al., who produced $Ni_{0.5}Fe_{0.5}$ thin film electrodes by thermal evaporation, the aged cluster electrode shows a comparable overpotential, although 4 to 5 times less material is used in our work [23]. The calculated TOF for the $Ni_{0.5}Fe_{0.5}$ cluster-based electrode is comparable to those of thin film catalysts previously reported in literature (Table 1). The TOF is in the same range as the $Ni_{0.9}Fe_{0.1}O_x$ electrode reported by Trotochaud et al., where directly mixed metal oxide films were produced. They report a TOF value of 0.21 s^{-1} consistent with the measured value of 0.21 s^{-1} for the $Ni_{0.5}Fe_{0.5}$ clusters measured after aging. We note however that our value is calculated from a CV at 10 mV s^{-1} and does not reflect the steady-state TOF value as in the case of Trotochaud et al., who used chronopotentiometry steps held for at least 15 min. Qiu et al. measured the OER activity of 4 nm amorphous Ni − Fe nanoparticles supported on carbon black and report a TOF of 0.2 s^{-1}.

Table 1
Comparison of $Ni_{0.5}Fe_{0.5}$ cluster electrode with catalyst activity of low metal loading electrodes published in recent years. For all measurements, the electrolyte was 1 M KOH. Data with a * are calculated by us, for mass calculations this was based on total amount of metal; # based on mass of entire oxide/oxyhydroxide film; § calculated from steady-state Tafel analysis; + use of rotating disk electrode; ++ cyclic voltammetry at 10 mV s^{-1} after the second 12 h chronopotentiometry experiment; c.d = chemical deposition technique; p.d = physical deposition technique.

	Method	Mass (μg/cm^2)	η (mV) at 10 mA/cm^2)	TOF (s^{-1}) η = 300 mV)	reference
$Ni_{0.5}Fe_{0.5}$ clusters on FTO	Gas-phase laser ablation (p.d.)	0.17*	372	0.04§/0.21++	This work
1 nm dense metallic $Ni_{0.5}Fe_{0.5}$ film on FTO	Thermal evaporation (p.d.)	*ca.* 0.83*	370	–	[23]
$Ni_{0.9}Fe_{0.1}O_x$ film on Au QCM	Spin casting + annealing (c.d.)	1.17 ± 0.14#	336§	0.21 ± 0.03§	[2]
4 nm $Ni_{0.69}Fe_{0.31}O_x$ particles on carbon	Organic solution phase reduction (c.d.)	*ca.* 23*	280+	0.2+	[9]
$Ni_{0.8}Fe_{0.2}O_xH_y$ film on Au QCM	Electrodeposition (c.d.)	4–5#	339*§	0.033§	[14]

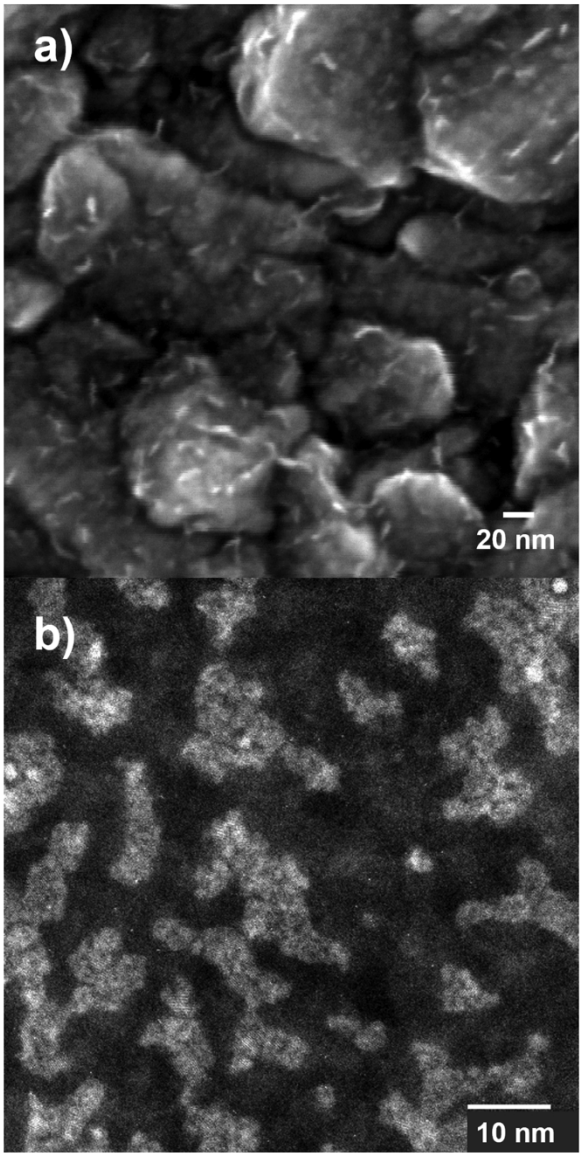

Fig. 5. SEM and HAADF-STEM images of the $Ni_{0.5}Fe_{0.5}$ clusters showing the effect of electrochemical cycling: a) SEM image of clusters on FTO and b) HAADF-STEM image on Au/C TEM grid.

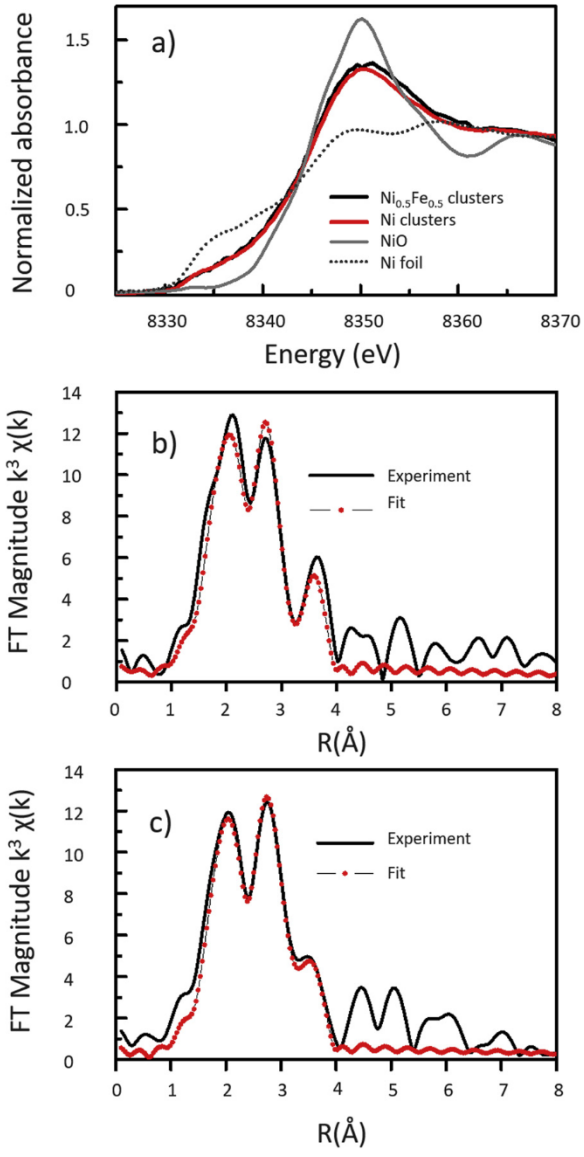

Fig. 6. a) XANES of as-deposited Ni and $Ni_{0.5}Fe_{0.5}$ clusters at Ni K edge along with Ni foil and NiO reference. b and c) Fourier Transform of fluorescence-detected Ni K-edge k^3-weighted EXAFS b) best fits of $Ni_{0.5}Fe_{0.5}$ clusters deposited on SiO_2/Si c) best fits of pure Ni clusters deposited on SiO_2/Si.

3.4. Structural characterization

To better understand the correlation between the increase in OER activity with aging and the structure and composition of the catalyst, an intensive structural characterization of the clusters was performed. After oxidation of the starting material and OER reaction, a structural reconfiguration of the $Ni_{0.5}Fe_{0.5}$ clusters occurs, as revealed by in-lens SEM and HAADF-STEM of clusters respectively deposited on FTO and Au/C TEM grid (Fig. 5a and b). Clusters are observed to aggregate in elongated islands of 20–40 nm length and to lose crystallinity. This means a strong rearrangement occurs throughout the whole structure of the clusters during OER. Counterintuitively, this did not coincide with a net decrease in catalytic activity.

Extensive investigation of the atomic and electronic structure and composition of as-deposited bimetallic $Ni_{0.5}Fe_{0.5}$ clusters on a SiO_2/Si substrate was carried out by a combination of bulk X-ray absorption near-edge structure (XANES) and extended X-ray absorption fine structure (EXAFS) at Ni K-edge. Pure Ni clusters, Ni foil and NiO were used as reference. Before and after the catalytic OER reaction NiFe clusters were investigated ex situ by surface sensitive XPS spectroscopies.

XANES spectra of pure Ni and mixed $Ni_{0.5}Fe_{0.5}$ clusters presented in Fig. 6a along with Ni foil and NiO references show nearly identical profiles lying between those of the 2 references, suggesting that both clusters consist of a mixture of metallic and oxidic phases. This demonstrates that mixing an equal amount Ni and Fe atoms does not significantly affect the local structure and the oxidation state of Ni atoms.

The EXAFS regions of the spectra were also analyzed. The best fits of the phase-corrected Fourier Transforms (FTs) of the χ(k) k^3-weighted EXAFS of mixed $Ni_{0.5}Fe_{0.5}$ and pure Ni clusters (Figs. S3 and S4 in Supplementary respectively) are shown in Fig. 6b and c. The structural parameters are listed in Table S1 in the Supplementary Information. Both FTs show mainly a double peak in the 1 to 4 Å range. This doublet was fitted with a first O contribution (N_1) consisting of 2.1 to 2.5 O at 1.97–1.98 Å in pure Ni and mixed $Ni_{0.5}Fe_{0.5}$ clusters respectively, indicating that a respective fraction of ca. 35 to 42% (2.1/6 and 2.5/6 - Ni in an octahedral oxygen coordination) of Ni atoms in these clusters is oxidized. The short oxide bond distances (1.97–1.98 Å) suggests a

possible mixture of NiO (Ni-O 2.08 Å), β-$Ni(OH)_2$ (Ni-O 2.06 Å) and β-NiOOH (Ni-O 1.9 and 2.07 Å) in both clusters. The second peak in the doublet corresponds to a shell (N_2) of 1.7 Ni atoms at 2.47 Å in pure Ni and 2.49 Å in mixed clusters respectively. An additional third shell of 0.7 Fe atoms at 2.49 Å (N_3) could be included in the $Ni_{0.5}Fe_{0.5}$ system. These distances that correspond closely to the typical Ni-Ni distances found in metallic nickel (2.48 Å in ref [52]) indicate the presence of a fraction of *ca.* 65% of a pure metallic phase in pure Ni clusters and *ca.* 58% of a Ni-rich NiFe alloy in the mixed clusters. Finally, the fit was completed by 1.9 -1.8 Ni at 2.91 Å (N_4) and 2.4 - 2.3 Ni at 3.41–3.45 Å (N_5) in both clusters. The first contribution may correspond to the average of the Ni-Ni distance found in NiO (2.95 Å) and in Ni oxyhydroxide (2.86 Å) and the latter one to the second neighbor shell Ni-Ni distances in Ni metal (3.45 Å) respectively [52–54]. The average size of the metallic core calculated from metal coordination number (CN) corrected by the corresponding sample metal fraction, CN_2 (1.7/0.65 = 2.6) in pure Ni clusters and $CN_{2+}CN_3$ (2.4/0.58 = 4.1) in $Ni_{0.5}Fe_{0.5}$ is below one nm.

X-ray photoelectron spectroscopy (XPS) was used to obtain binding energies of Ni 2p and Fe 2p core levels of the $Ni_{0.5}Fe_{0.5}$ clusters on Au/Si. The XPS spectra of Ni 2p, Fe 2p and O 1 s of the clusters are shown in Fig. 7. The top and bottom row show respectively the spectra before and after a few CV cycles. As depicted in Fig. 7a, the peak around 855.2 eV is assigned to Ni $2p_{3/2}$ of Ni^{2+}, associated to $Ni(OH)_2$, while the peak around 856.5 eV is assigned to Ni^{3+} of NiOOH [55–57]. The peak at ~859 eV is assigned to a higher oxidation state or a combination of the shake-up features of the $Ni(OH)_2$ and NiOOH peaks. Before reaction, the abundance of $Ni(OH)_2$ is slightly higher than NiOOH ($I_{Ni(OH)_2}$: $I_{NiOOH:}$ = 1: 0.7), while after reaction the abundance of NiOOH becomes higher than $Ni(OH)_2$ ($I_{Ni(OH)_2}$: $I_{NiOOH:}$ = 1: 4.7). The transformation of the as-deposited metallic to the (oxy)hydroxide phase is thus confirmed by XPS. This is also corroborated by the O 1 s peaks observed at ~530.6 eV and 531.8 eV, respectively assigned to $Ni(OH)_2$ and NiOOH [56,58]. No peak related to NiO phase (around 529.3 eV) could be observed [58,59]. After reaction a large water peak was visible in the O 1 s spectrum [56]. While the same phases are present at the surface of the sample after reaction, a remarkable change of their relative abundance is observed as NiOOH becomes dominant at the expense of Ni $(OH)_2$.

Also in the Fe 2p spectrum no metallic peak is visible (706.7 eV) [60–62]. Two peaks around 710.8 and 712 eV, related to Fe $2p_{3/2}$ of Fe^{3+}, are respectively indicative of the presence of Fe_2O_3 and FeOOH phases [63,64]. The broad peak and close lying binding energies make it difficult to differentiate between FeOOH and Fe_2O_3 [65]. Also a small peak around 709.6 eV is visible and was associated to a FeO phase [60]. After reaction the Fe peak fell below detection limits due to the low loading. Because of the low signal-to-noise ratio, it is possible that the Fe peak is buried in the noise level and therefore, the detection limit could be above 5 to 10% Fe [66,67]. The disappearance of the Fe peak may originate from a rearrangement of the two elements within the clusters during the reaction, resulting in enrichment in Ni (NiOOH) cluster surface and a Fe rich core. Due to the limited penetration depth the Fe 2p peak would be invisible. For pure Fe material, the inelastic mean free path of an electron is less than 1 nm for the kinetic energy that was considered by us [68]. Another plausible explanation is the leaching of iron from the surface, which is supported by reports in literature where depletion of Fe under OER reaction in KOH is observed [65,69,70].

Combination of the results obtained by the bulk high-energy XAFS and surface low-energy XPS x-ray spectroscopies show that upon exposure to the ambient, the pure Ni and NiFe alloy metallic clusters are partially oxidized into NiO that is then hydrated into Ni hydroxide Ni $(OH)_2$ and further oxidized into oxyhydroxide (NiOOH) phases. The layered structure of the NiFe clusters is supported by the absence of peaks related either to Ni metallic or to the dry NiO oxide in the XPS analysis. This confirms that these two phases are never located at the surface of the clusters but systematically forming their core. XPS in agreement with the EXAFS analysis shows that the outer surface of the particles consists of $Ni(OH)_2$ and NiOOH. Under OER conditions in 1 M KOH, the NiOOH layer grows and becomes the dominant surface phase. This would be in line with reports that identified NiOOH as the formed phase under OER conditions [33,34]. The role of Fe in the Ni phase transformation is unclear. Although it forms the NiFe alloy and a segregated FeOOH phase respectively in the core and at the surface of the non-reacted sample, it seems to fall below the XPS detection limit in the reacted samples. Previous studies in purified electrolyte without Fe impurities show that pure NiOOH has a low activity, which indicated that the activity is strongly related with the incorporation of iron from the electrolyte [2,5,7]. Fe is essential for high OER activities and is reported to be the active site [7,34]. Using operando X-ray absorption spectroscopy and computational methods, Friebel et al. demonstrated that Fe is the active site for OER in the $Ni_xFe_{1-x}OOH$ system [6]. Therefore we hypothesize that a small amount of iron that falls below

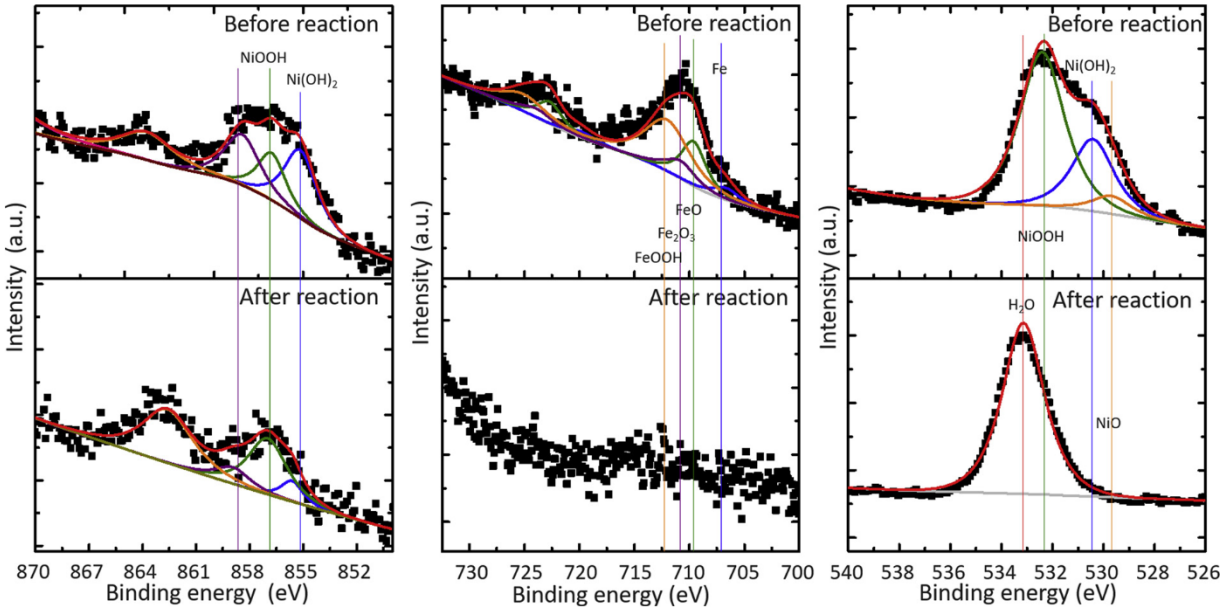

Fig. 7. Comparison of the Ni 2p3/2, Fe 2p3/2 and O 1 s spectra of $Ni_{0.5}Fe_{0.5}$ clusters on Au/Si before and after a few CV cycles.

the detection limit of XPS, is still present after leaching.

4. Conclusions

We have shown the validity and benefits of the CBD technology in the preparation of model OER electrodes. This technique can deposit highly dispersed NiFe clusters with controlled size, composition and coverage on FTO substrate. The $Ni_{0.5}Fe_{0.5}$ clusters have shown surprisingly high intrinsic OER activity given the ultra-low mass loading. Our electrodes with NiFe clusters perform in the same range of the highest intrinsic OER activities till now reported for NiFe thin films and nanostructures, although a much lower amount of active catalyst was used. Electrochemical aging significantly increases the OER performance. Reexamination by SEM after OER shows a structural rearrangement and strong aggregation. Detailed XPS analysis after OER shows disappearance of the binding energies in the Fe 2p zone, while in the Ni 2p zone a large peak assigned to NiOOH was measured. Aging may be related to the formation of a NiOOH phase at the cluster surface observed by XAFS and XPS spectroscopies. The role of Fe in the higher activity of mixed NiFe clusters is unclear as it seems to disappear from the cluster surface after aging. Due to the promising results obtained by this study, further work, in which different compositions can be screened combined with in situ spectroscopic characterization, is expected to improve the understanding of structural and compositional effects on NiFe electrocatalyst activity.

Declarations of interest

None.

Acknowledgments

This work is supported by Research Foundation Flanders (G0A5417N) and the Flemish Government through Long-term structural funding (Methusalem) and European Union's Seventh Framework Programme (FP7/2007-2013) under grant agreement n° 607417 (CATSENSE). JR is a postdoctoral fellow of the Research Foundation – Flanders. It was also supported by the Flemish Hercules Stichting project (AKUL/13/19 and AKUL/13/24). The authors gratefully acknowledge financial support from the Research Foundation Flanders (FWO) grant (G.0B39.15). Access to DUBBLE (26-01-1113) was arranged through the support of FWO for use of the central facilities. The authors thank the staff of beamlines of the ESRF for their assistance and technical support and prof. Jin Won Seo for assistance in STEM.

Appendix A. Supplementary data

Supplementary material related to this article can be found, in the online version, at doi:https://doi.org/10.1016/j.cattod.2019.01.062.

References

[1] F. Dionigi, P. Strasser, NiFe-based (oxy)hydroxide catalysts for oxygen evolution reaction in non-acidic electrolytes, Adv. Energy Mater. 6 (2016) 1600621, https://doi.org/10.1002/aenm.201600621.

[2] L. Trotochaud, J.K. Ranney, K.N. Williams, S.W. Boettcher, Solution-cast metal oxide thin film electrocatalysts for oxygen evolution, J. Am. Chem. Soc. 134 (2012) 17253–17261, https://doi.org/10.1021/ja307507a.

[3] F. Song, X. Hu, Exfoliation of layered double hydroxides for enhanced oxygen evolution catalysis, Nat. Commun. 5 (2014) 4477, https://doi.org/10.1038/ncomms5477.

[4] J. Qi, W. Zhang, R. Xiang, K. Liu, H.Y. Wang, M. Chen, Y. Han, R. Cao, Porous nickel–iron oxide as a highly efficient electrocatalyst for oxygen evolution reaction, Adv. Sci. 2 (2015) 1500199, https://doi.org/10.1002/advs.201500199.

[5] L. Trotochaud, S.L. Young, J.K. Ranney, S.W. Boettcher, Nickel-iron oxyhydroxide oxygen-evolution electrocatalysts: the role of intentional and incidental Iron incorporation, J. Am. Chem. Soc. 136 (2014) 6744–6753, https://doi.org/10.1021/ja502379c.

[6] D. Friebel, M.W. Louie, M. Bajdich, K.E. Sanwald, Y. Cai, A.M. Wise, M.J. Cheng, D. Sokaras, T.C. Weng, R. Alonso-Mori, R.C. Davis, J.R. Bargar, J.K. Nørskov, A. Nilsson, A.T. Bell, Identification of highly active Fe sites in (Ni,Fe)OOH for electrocatalytic water splitting, J. Am. Chem. Soc. 137 (2015) 1305–1313, https://doi.org/10.1021/ja511559d.

[7] M.S. Burke, L.J. Enman, A.S. Batchellor, S. Zou, S.W. Boettcher, Oxygen evolution reaction electrocatalysis on transition metal oxides and (oxy)hydroxides: activity trends and design principles, Chem. Mater. 27 (2015) 7549–7558, https://doi.org/10.1021/acs.chemmater.5b03148.

[8] M. Gong, H. Dai, A mini review of NiFe-based materials as highly active oxygen evolution reaction electrocatalysts, Nano Res. 8 (2015) 23–39, https://doi.org/10.1007/s12274-014-0591-z.

[9] Y. Qiu, L. Xin, W. Li, Electrocatalytic oxygen evolution over supported small amorphous ni-fe nanoparticles in alkaline electrolyte, Langmuir 30 (2014) 7893–7901, https://doi.org/10.1021/la501246e.

[10] M.W. Louie, A.T. Bell, An investigation of thin-film Ni − Fe oxide catalysts for the electrochemical evolution of oxygen, J. Am. Chem. Soc. 135 (2013) 12329–12337, https://doi.org/10.1021/ja405351s.

[11] J.Y.C. Chen, L. Dang, H. Liang, W. Bi, J.B. Gerken, S. Jin, E.E. Alp, S.S. Stahl, Operando analysis of NiFe and Fe oxyhydroxide electrocatalysts for water oxidation: detection of Fe4+ by mössbauer spectroscopy, J. Am. Chem. Soc. 137 (2015) 15090–15093, https://doi.org/10.1021/jacs.5b10699.

[12] D.A. Corrigan, The catalysis of the oxygen evolution reaction by Iron impurities in thin film nickel oxide electrodes, J. Electrochem. Soc. 134 (1987) 377, https://doi.org/10.1149/1.2100463.

[13] X. Li, F.C. Walsh, D. Pletcher, Nickel based electrocatalysts for oxygen evolution in high current density, alkaline water electrolysers, Phys. Chem. Chem. Phys. 13 (2011) 1162–1167, https://doi.org/10.1039/c0cp00993h.

[14] M.B. Stevens, L.J. Enman, A.S. Batchellor, M.R. Cosby, A.E. Vise, C.D.M. Trang, S.W. Boettcher, Measurement techniques for the study of thin film heterogeneous water oxidation electrocatalysts, Chem. Mater. 29 (2017) 120–140, https://doi.org/10.1021/acs.chemmater.6b02796.

[15] Z.K. Goldsmith, A.K. Harshan, J.B. Gerken, M. Vörös, G. Galli, S.S. Stahl, S. Hammes-Schiffer, Characterization of NiFe oxyhydroxide electrocatalysts by integrated electronic structure calculations and spectroelectrochemistry, Proc. Natl. Acad. Sci. 114 (2017) 3050–3055, https://doi.org/10.1073/pnas.1702081114.

[16] D. Jeong, K. Jin, S.E. Jerng, H. Seo, D. Kim, S.H. Nahm, S.H. Kim, K.T. Nam, Mn 5 O_8 nanoparticles as efficient water oxidation catalysts at neutral pH, ACS Catal. 5 (2015) 4624–4628, https://doi.org/10.1021/acscatal.5b01269.

[17] X. Lu, C. Zhao, Electrodeposition of hierarchically structured three-dimensional nickel–iron electrodes for efficient oxygen evolution at high current densities, Nat. Commun. 6 (2015) 6616, https://doi.org/10.1038/ncomms7616.

[18] J. Wang, W. Cui, Q. Liu, Z. Xing, A.M. Asiri, X. Sun, Recent progress in cobalt-based heterogeneous catalysts for electrochemical water splitting, Adv. Mater. 28 (2016) 215–230, https://doi.org/10.1002/adma.201502696.

[19] J. Zhao, X. Li, G. Cui, X. Sun, Highly-active oxygen evolution electrocatalyzed by an Fe-doped NiCr2O4 nanoparticle film, Chem. Commun. 54 (2018) 5462–5465, https://doi.org/10.1039/c8cc02568a.

[20] D. Xu, M.B. Stevens, Y. Rui, G. DeLuca, S.W. Boettcher, E. Reichmanis, Y. Li, Q. Zhang, H. Wang, The role of Cr doping in Ni–Fe oxide/(oxy)hydroxide electrocatalysts for oxygen evolution, Electrochim. Acta 265 (2018) 10–18, https://doi.org/10.1016/j.electacta.2018.01.143.

[21] M.P. Browne, J.M. Vasconcelos, J. Coelho, M. O'Brien, A.A. Rovetta, E.K. McCarthy, H. Nolan, G.S. Duesberg, V. Nicolosi, P.E. Colavita, M.E.G. Lyons, Improving the performance of porous nickel foam for water oxidation using hydrothermally prepared Ni and Fe metal oxides, Sustain. Energy Fuels (2017) 207–216, https://doi.org/10.1039/C6SE00032K.

[22] E.L. Miller, Richard E. Rocheleau, Electrochemical behavior of reactively sputtered iron-doped nickel oxide, J. Electrochem. Soc. 144 (1997) 3072, https://doi.org/10.1149/1.1837961.

[23] M. Biset-Peiró, S. Murcia-López, C. Fàbrega, J.R. Morante, T. Andreu, Multilayer Ni/Fe thin films as oxygen evolution catalysts for solar fuel production, J. Phys. D: Appl. Phys. 50 (2017) 104003, https://doi.org/10.1088/1361-6463/aa562b.

[24] M. Plata-Torres, A.M. Torres-Huerta, M.A. Domínguez-Crespo, E.M. Arce-Estrada, C. Ramírez-Rodríguez, Electrochemical performance of crystalline Ni-Co-Mo-Fe electrodes obtained by mechanical alloying on the oxygen evolution reaction, Int. J. Hydrogen Energy 32 (2007) 4142–4152, https://doi.org/10.1016/j.ijhydene.2007.05.023.

[25] J.Y.C. Chen, J.T. Miller, J.B. Gerken, S.S. Stahl, Inverse spinel NiFeAlO4 as a highly active oxygen evolution electrocatalyst: promotion of activity by a redox-inert metal ion, Energy Environ. Sci. 7 (2014) 1382, https://doi.org/10.1039/c3ee43811b.

[26] Z. Zhang, Y. Liu, G. Yao, G. Zu, Y. Hao, Synthesis and characterization of NiFe2O4 nanoparticles via solid-state reaction, Int. J. Appl. Ceram. Technol. 10 (2013) 142–149, https://doi.org/10.1111/j.1744-7402.2011.02719.x.

[27] B.M. Hunter, J.D. Blakemore, M. Deimund, H.B. Gray, J.R. Winkler, A.M. Müller, Highly active mixed-metal nanosheet water oxidation catalysts made by pulsed-laser ablation in liquids, J. Am. Chem. Soc. 136 (2014) 13118–13121, https://doi.org/10.1021/ja506087h.

[28] L. Kuai, J. Geng, C. Chen, E. Kan, Y. Liu, Q. Wang, B. Geng, A reliable aerosol-spray-assisted approach to produce and optimize amorphous metal oxide catalysts for electrochemical water splitting, Angew. Chem. - Int. Ed. 53 (2014) 7547–7551, https://doi.org/10.1002/anie.201404208.

[29] R.D.L. Smith, M.S. Prévot, R.D. Fagan, Z. Zhang, P.A. Sedach, M.K.J. Siu, S. Trudel, C.P. Berlinguette, Photochemical route for accessing amorphous metal oxide Materials for water oxidation Catalysis, Science 340 (2013) 60–63.

[30] S. Zou, M.S. Burke, M.G. Kast, J. Fan, N. Danilovic, S.W. Boettcher, Fe (Oxy)hydroxide oxygen evolution reaction electrocatalysis: intrinsic activity and the roles of

electrical conductivity, substrate, and dissolution, Chem. Mater. 27 (2015) 8011–8020, https://doi.org/10.1021/acs.chemmater.5b03404.
[31] M. Favaro, W.S. Drisdell, M.A. Marcus, J.M. Gregoire, E.J. Crumlin, J.A. Haber, J. Yano, An operando investigation of (Ni-Fe-Co-Ce)Ox system as highly efficient electrocatalyst for oxygen evolution reaction, ACS Catal. 7 (2017) 1248–1258, https://doi.org/10.1021/acscatal.6b03126.
[32] B.S. Yeo, A.T. Bell, In situ raman study of nickel oxide and gold-supported nickel oxide catalysts for the electrochemical evolution of oxygen, J. Phys. Chem. C 116 (2012) 8394–8400, https://doi.org/10.1021/jp3007415.
[33] M.S. Burke, S. Zou, L.J. Enman, J.E. Kellon, C.A. Gabor, E. Pledger, S.W. Boettcher, Revised oxygen evolution reaction activity trends for first-row transition-metal (Oxy)hydroxides in alkaline media, J. Phys. Chem. Lett. 6 (2015) 3737–3742, https://doi.org/10.1021/acs.jpclett.5b01650.
[34] S. Klaus, Y. Cai, M.W. Louie, L. Trotochaud, A.T. Bell, Effects of Fe electrolyte impurities on Ni(OH)2/NiOOH structure and oxygen evolution activity, J. Phys. Chem. C 119 (2015) 7243–7254, https://doi.org/10.1021/acs.jpcc.5b00105.
[35] L. Trotochaud, Structure-Composition-Activity Relationships in Transition-Metal Oxide and Oxyhydroxide Oxygen-Evolution Electrocatalysts, University of Oregon Graduate School, 2014.
[36] B. Zhang, Y.H. Lui, H. Ni, S. Hu, Bimetallic (FexNi1 − x)2P nanoarrays as exceptionally efficient electrocatalysts for oxygen evolution in alkaline and neutral media, Nano Energy 38 (2017) 553–560, https://doi.org/10.1016/j.nanoen.2017.06.032.
[37] N. Cheng, Q. Liu, J. Tian, Y. Xue, A.M. Asiri, H. Jiang, Y. He, X. Sun, Acidically oxidized carbon cloth: a novel metal-free oxygen evolution electrode with high catalytic activity, Chem. Commun. 51 (2015) 1616–1619, https://doi.org/10.1039/c4cc07120d.
[38] J. Tian, Q. Liu, A.M. Asiri, X. Sun, Self-Supported Nanoporous Cobalt Phosphide Nanowire Arrays: An Efficient 3D Hydrogen-Evolving Cathode over the Wide Range of pH 0–14, J. Am. Chem. Soc. 136 (2014) 7587–7590, https://doi.org/10.1021/ja503372r.
[39] N. Vandamme, E. Janssens, F. Vanhoutte, P. Lievens, C. Van Haesendonck, Scanning probe microscopy investigation of gold clusters deposited on atomically flat substrates, J. Phys. Condens. Matter 15 (2003) S2983–S2999, https://doi.org/10.1088/0953-8984/15/42/001.
[40] W. Bouwen, P. Thoen, F. Vanhoutte, S. Bouckaert, F. Despa, H. Weidele, R.E. Silverans, P. Lievens, Production of bimetallic clusters by a dual-target dual-laser vaporization source, Rev. Sci. Instrum. 71 (2000) 54–58, https://doi.org/10.1063/1.1150159.
[41] T.W. Liao, A. Yadav, K.J. Hu, J. Van Der Tol, S. Cosentino, F. D'Acapito, R.E. Palmer, C. Lenardi, R. Ferrando, D. Grandjean, P. Lievens, Unravelling the nucleation mechanism of bimetallic nanoparticles with composition-tunable core-shell arrangement, Nanoscale 10 (2018) 6684–6694, https://doi.org/10.1039/c8nr01481g.
[42] E.C. Tyo, S. Vajda, Catalysis by clusters with precise numbers of atoms, Nat. Nanotechnol. 10 (2015) 577–588, https://doi.org/10.1038/nnano.2015.140.
[43] S. Vajda, M.G. White, Catalysis applications of size-selected cluster deposition, ACS Catal. 5 (2015) 7152–7176, https://doi.org/10.1021/acscatal.5b01816.
[44] M. Borsboom, W. Bras, I. Cerjak, D. Detollenaere, D. Glastra Van Loon, P. Goedtkindt, M. Konijnenburg, P. Lassing, Y.K. Levine, B. Munneke, M. Oversluizen, R. Van Tol, E. Vlieg, The dutch-belgian beamline at the ESRF, J. Synchrotron Radiat. 5 (1998) 518–520, https://doi.org/10.1107/S0909049597013484.
[45] N. Binsted, J. Campbell, S.J. Gurman, P.C. Stephenson, EXAFS Analysis Programs Daresbury Laboratory, Warrington, U.K. (1991).
[46] M. Mayer, SIMNRA User's Guide, Report IPP 9/113, Max-planck-Institut Für Plasmaphysik, Garching, Germany (1997).
[47] M.E.G. Lyons, Michael P. Brandon, The oxygen evolution reaction on passive oxide covered transition metal electrodes in aqueous alkaline solution. Part 1-nickel, Int. J. Electrochem. Sci. 3 (2008) 1386–1424.
[48] M. Wehrens-Dijksma, P.H.L. Notten, Electrochemical quartz microbalance characterization of Ni(OH)2-based thin film electrodes, Electrochim. Acta 51 (2006) 3609–3621, https://doi.org/10.1016/j.electacta.2005.10.022.
[49] I.J. Godwin, M.E.G. Lyons, Enhanced oxygen evolution at hydrous nickel oxide electrodes via electrochemical ageing in alkaline solution, Electrochem. Commun. 32 (2013) 39–42, https://doi.org/10.1016/j.elecom.2013.03.040.
[50] M. Görlin, P. Chernev, J.F. De Araújo, T. Reier, S. Dresp, B. Paul, R. Krähnert, H. Dau, P. Strasser, Oxygen evolution reaction dynamics, faradaic charge efficiency, and the active metal redox states of Ni-Fe oxide water splitting electrocatalysts, J. Am. Chem. Soc. 138 (2016) 5603–5614, https://doi.org/10.1021/jacs.6b00332.
[51] C.C.L. McCrory, S.H. Jung, J.C. Peters, T.F. Jaramillo, Benchmarking heterogeneous electrocatalysts for the oxygen evolution reaction, J. Am. Chem. Soc. 135 (2013) 16977–16987, https://doi.org/10.1021/ja407115p.
[52] A.N. Mansour, C.A. Melendres, X-ray absorption spectra and structure of some nickel oxides (hydroxides), Electrochem. Soc. Ext. Abstr. 94–2 (1994).
[53] A.N. Mansour, C.A. Melendres, XAFS investigation of the structure and valency of nickel in some oxycompounds, Phys. B Phys. Condens. Matter. 208–209 (1995) 583–584, https://doi.org/10.1016/0921-4526(94)00761-J.
[54] A.N. Mansour, C.A. Melendres, M. Pankuch, R.A. Brizzolara, X-ray absorption fine structure spectra and the oxidation state of nickel in some of its oxycompounds, J. Electrochem. Soc. 141 (1994) L69, https://doi.org/10.1149/1.2054990.
[55] K. Lian, S.J. Thorpe, D.W. Kirk, Electrochemical and surface characterization of electrocatalytically active amorphous NiCo alloys, Electrochim. Acta 37 (1992) 2029–2041, https://doi.org/10.1016/0013-4686(92)87119-K.
[56] E.L. Ratcliff, J. Meyer, K.X. Steirer, A. Garcia, J.J. Berry, D.S. Ginley, D.C. Olson, A. Kahn, N.R. Armstrong, Evidence for near-surface NiOOH species in solution-processed NiOxselective interlayer materials: impact on energetics and the performance of polymer bulk heterojunction photovoltaics, Chem. Mater. 23 (2011) 4988–5000, https://doi.org/10.1021/cm202296p.
[57] M.C. Biesinger, L.W.M. Lau, A.R. Gerson, R.S.C. Smart, The role of the Auger parameter in XPS studies of nickel metal, halides and oxides, Phys. Chem. Chem. Phys. 14 (2012) 2434–2442, https://doi.org/10.1039/c2cp22419d.
[58] A.N. Mansour, Characterization of β-Ni(OH)2 by XPS, Surf. Sci. Spectra 3 (1994) 239, https://doi.org/10.1116/1.1247752.
[59] M.C. Biesinger, B.P. Payne, L.W.M. Lau, A. Gerson, R.S.C. Smart, X-ray photoelectron spectroscopic chemical state quantification of mixed nickel metal, oxide and hydroxide systems, Surf. Interface Anal. 41 (2009) 324–332, https://doi.org/10.1002/sia.3026.
[60] P. Mills, J.L. Sullivan, A study of the core level electrons in iron and its three oxides by means of x-ray photoelectron spectroscopy, J. Phys. D Appl. Phys. 16 (1983) 723–732, https://doi.org/10.1088/0022-3727/16/5/005.
[61] S. Oida, F.R. McFeely, A.A. Bol, X-ray photoelectron spectroscopy study on Fe and Co catalysts during the first stages of ethanol chemical vapor deposition for single-walled carbon nanotube growth, J. Appl. Phys. 109 (2011) 064304, https://doi.org/10.1063/1.3552306.
[62] J.F. Moulder, W.F. Stickle, P.E. Sobol, K.D. Bomben, Handbook of X-ray Photoelectron Spectroscopy: A Reference Book of Standard Spectra for Identification and Interpretation of XPS Data, (1992) 9780962702624.
[63] X. Hu, J.C. Yu, J. Gong, Q. Li, G. Li, A-Fe2O3 nanorings prepared by a microwave-assisted hydrothermal process and their sensing properties, Adv. Mater. 19 (2007) 2324–2329, https://doi.org/10.1002/adma.200602176.
[64] B.J. Tan, K.J. Klabunde, Peter M.A. Sherwood, X-ray photoelectron spectroscopy studies of solvated metal atom dispersed catalysts. Monometallic iron and bimetallic iron-cobalt particles on alumina, Chem. Mater. 2 (1990) 186–191, https://doi.org/10.1021/cm00008a021.
[65] B. Sebok, Creating Model Systems for Catalysis With Mass-selected Nanoparticles, Technical University of Denmark, 2017.
[66] N. Fairly, CasaXPS Manual 2.3.15 Introduction to XPS and AES, Casa Softw. Ltd, 2009, pp. 1–177.
[67] N. Weidler, J. Schuch, F. Knaus, P. Stenner, S. Hoch, A. Maljusch, R. Schäfer, B. Kaiser, W. Jaegermann, X-ray photoelectron spectroscopic investigation of plasma-enhanced chemical vapor deposited NiO_x, $NiO_x(OH)_y$, and $CoNiO_x(OH)_y$: influence of the chemical composition on the catalytic activity for the oxygen evolution reaction, J. Phys. Chem. C 121 (2017) 6455–6463, https://doi.org/10.1021/acs.jpcc.6b12652.
[68] C.J. Powell, A. Jablonski, NIST Electron Inelastic-Mean-Free-Path Database - Version 1.2, National Institute of Standards and Technology, Gaithersburg, MD, 2010.
[69] F.D. Speck, K.E. Dettelbach, R.S. Sherbo, D.A. Salvatore, A. Huang, C.P. Berlinguette, On the electrolytic stability of iron-nickel oxides, Chem 2 (2017) 590–597, https://doi.org/10.1016/j.chempr.2017.03.006.
[70] J. Xu, J. Li, D. Xiong, B. Zhang, Y. Liu, K.H. Wu, I. Amorim, W. Li, L. Liu, Trends in activity for the oxygen evolution reaction on transition metal (M = Fe, Co, Ni) phosphide pre-catalysts, Chem. Sci. 9 (2018) 3470–3476, https://doi.org/10.1039/c7sc05033j.